

DOI: 10.1002/adem.201600020

# Active Cooling of a Microvascular Shape Memory Alloy-Polymer Matrix Composite Hybrid Material\*\*

By Anthony M. Coppola, Liangfa Hu, Piyush R. Thakre,<sup>1</sup> Miladin Radovic, Ibrahim Karaman, Nancy R. Sottos and Scott R. White\*

*Microvascular shape memory alloy (SMA)-polymer matrix composite (PMC) hybrid materials are fabricated using the Vaporization of Sacrificial Components (VaSC) technique. Two types of sacrificial materials are used: Mg wires in the SMA (nickel titanium) and poly(lactic acid)/tin(II) oxalate fibers in the PMC (glass fiber/epoxy). These sacrificial materials survive the initial solidification of the host materials, then are vaporized during a final thermal treatment to reveal the vascular network. The effect of VaSC on composition and transformation temperatures of the SMA are examined. Active cooling through the vascular network maintains temperature in the PMC below the glass transition temperature (152 °C) at heat fluxes as high as 300 kW m<sup>-2</sup>, while this temperature is exceeded without cooling at just 10 kW m<sup>-2</sup>.*

## 1. Introduction

Future aerospace vehicles call for multifunctional composite materials to survive the extreme mechanical and thermal loads experienced during hypersonic flights where incident heat fluxes reach several hundred kilowatt per meter square.<sup>[1]</sup> The layered hybrid composite structure shown in Figure 1 is an example of a multifunctional system designed for such applications. Each layer contributes properties suited to a particular task, including the thermal protection of the

oxide ceramic, mechanical damping and toughness of the shape memory alloy (SMA), and the high strength-to-weight ratio of the polymer matrix composite (PMC). However, exceedingly high temperatures occur without an integrated heat removal system. An internal vascular network can enable active thermal regulation, allowing for on-demand, adaptive heat removal and preservation of material properties. Active cooling systems are used extensively in electronics,<sup>[2]</sup> fuel cells,<sup>[3,4]</sup> high power batteries,<sup>[5]</sup> micro-electro-mechanical systems (MEMS),<sup>[6]</sup> and spacecraft systems.<sup>[7-9]</sup> In addition to cooling, vascular networks in PMCs enable self-healing,<sup>[10-13]</sup> electromagnetic modulation,<sup>[14]</sup> and damage detection.<sup>[15-17]</sup>

Here, we fabricate a vascular network into each phase of a bilayer nickel-titanium (NiTi)/glass fiber reinforced epoxy hybrid by the Vaporization of Sacrificial Components (VaSC) technique.<sup>[14,18,19]</sup> This hybrid material represents the bottom two layer of the proposed multilayer hybrid composite (Figure 1). The effects of VaSC on material composition and phase transformation of the NiTi SMA are examined. We then evaluate the cooling performance of the hybrid system under incident heat flux up to 300 kW m<sup>-2</sup>. The effects of channel distribution in each phase, coolant flow rate, and coolant media are also evaluated. Our technical objective is to maintain the temperature in each phase below the temperature threshold for degradation in mechanical properties, *ca.* 152 °C in the PMC and 500 °C in the SMA.

The PMC has excellent specific strength, specific stiffness, and fatigue life and provides the structural support for our hybrid material system. Soghrati et al.<sup>[20,21]</sup> and Phillips et al.<sup>[22]</sup> demonstrated the effectiveness of active cooling through channels in a PMC at minimal channel volume

[\*] Prof. S. R. White, Dr. A. M. Coppola

Aerospace Engineering Department, Beckman Institute for Advanced Science and Technology, University of Illinois at Urbana-Champaign, Urbana, Illinois 61801, USA  
E-mail: swhite@illinois.edu

Dr. L. Hu, Prof. M. Radovic, Prof. I. Karaman  
Department of Materials Science and Engineering, Texas A&M University, College Station, Texas 77843, USA

Dr. P. R. Thakre  
Beckman Institute for Advanced Science and Technology, University of Illinois at Urbana-Champaign, Urbana, Illinois 61801, USA

Prof. N. R. Sottos  
Materials Science and Engineering Department, Beckman Institute for Advanced Science and Technology, University of Illinois at Urbana-Champaign, Urbana, Illinois 61801, USA

<sup>1</sup> Present address: Dow Chemical Company, Midland, Michigan 48642, USA

[\*\*] (Supporting Information is available online from Wiley Online Library or from the author).

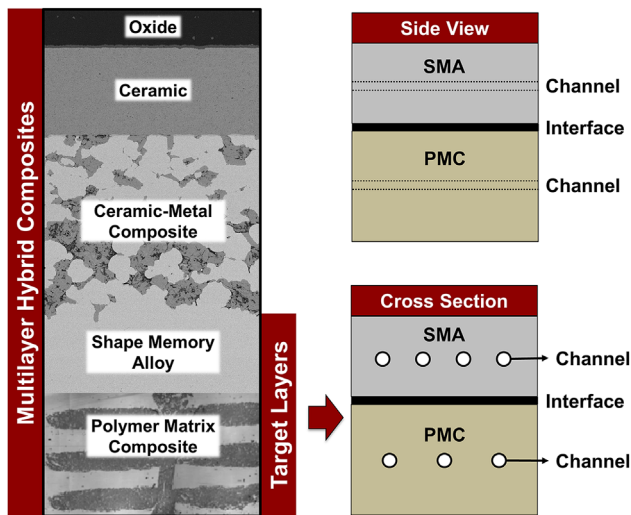


Fig. 1. (Left) Cross-sectional view of the proposed hybrid composite material system designed as a multifunctional structural skin for future hypersonic vehicles. (Right) Schematic view of the target layers under consideration in this study, including the vascularized SMA and PMC phases, joined by an interphase-bonding layer. Figure not to scale.

fractions (ca. 3% or less). However, in all cases PMCs were best suited for heat fluxes well below  $100 \text{ kW m}^{-2}$  due to the relatively low thermal conductivity of the host material. Many studies have examined the effect of channels on mechanical properties of a PMC, including compressive strength and stiffness,<sup>[23–25]</sup> fracture toughness,<sup>[22,26,27]</sup> and impact damage resistance,<sup>[28,29]</sup> demonstrating minimal adverse effect for low channel volume fractions (ca. <3%).

The NiTi SMA layer provides high mechanical damping and toughness through energy dissipation as a result of superelasticity,<sup>[30]</sup> and acts as an intermediate layer between the PMC and the ceramic-metal (NiTi) composite (CMC) in our multilayer hybrid composite. While superelasticity in equiatomic NiTi degrades around  $150^\circ\text{C}$ , Ni-rich alloys can demonstrate superelasticity up to  $220^\circ\text{C}$ <sup>[31]</sup> and high temperature SMAs of the type NiTiX (X=Hf, Zr, Pd, Pt, Au) up to  $500^\circ\text{C}$ .<sup>[30]</sup> Hu et al.,<sup>[32]</sup> and Kothalkar et al.,<sup>[33]</sup> have demonstrated several benefits of combining NiTi with carbide ceramics in a CMC, including the ability to control residual stresses through the constituent composition, phase morphology, and thermomechanical conditioning.<sup>[33]</sup> Vascularization of NiTi provides enhanced cooling capability compared to the PMC alone. The thermal conductivity of NiTi is in the range of  $12\text{--}16 \text{ W m}^{-1} \text{ K}^{-1}$ <sup>[34]</sup> (isotropic) compared to only  $0.4\text{--}0.6 \text{ W m}^{-1} \text{ K}^{-1}$  in the through-thickness direction for the PMC.<sup>[21]</sup>

The primary barrier to utilizing active cooling in many material systems is fabrication of the vascular network. Methods for fabricating vascular networks into PMCs include integration of hollow glass fibers,<sup>[17,23,35]</sup> removal of a solid wire through either melt or manual extraction,<sup>[13,26,28]</sup> and VaSC.<sup>[14,18]</sup> Unlike other methods, which are restricted to straight channels with one-dimensional connectivity,

sacrificial fibers used for VaSC allow for three-dimensional, interconnected architectures.<sup>[14]</sup>

To create vascular networks in NiTi SMA, a new VaSC process was developed inspired by a technique initially demonstrated for titanium<sup>[36]</sup> and Ti-6Al-4V.<sup>[37,38]</sup> Dunand et al. used steel wire meshes as a sacrificial template and removed the meshes electrochemically after densification of NiTi powders by hot-pressing.<sup>[39,40]</sup> Bansiddhi et al. used Nb wires as space holders in NiTi to create channels during sintering as the Nb reacted with the NiTi to create a eutectic liquid that wicked into the spaces in the NiTi.<sup>[41]</sup> Aydogmus et al. used magnesium (Mg) particles as a sacrificial material to fabricate porous titanium alloys and evaporated the particles during pressureless sintering.<sup>[42,43]</sup> Modeled on this work, Mg wires were used in the present work as the sacrificial material to create vascular channels in the NiTi SMA. Mg was selected because it is not soluble in Ti or Ni and provides a reducing atmosphere that prevents oxidation of NiTi during sintering.

## 2. Results and Discussion

### 2.1. Vascularization of the Hybrid SMA-PMC

Microchannels of  $500 \mu\text{m}$  diameter were created in the SMA and PMC using the VaSC procedures outlined in Figure 2. The VaSC procedure for each material includes integration of the vascular template into the precursor materials, manufacture of the bulk material, then removal of sacrificial materials to create the channels through a thermal treatment process. Images of the resulting channels are shown in Figure 2 confirming that the channels are round and free of residual material.

### 2.2. Post-VaSC Characterization of the SMA

Figure 3a shows the X-ray diffraction (XRD) patterns of the NiTi powder and bulk NiTi-as-sintered and solution heat treated. The NiTi powder consists of only austenite phase (B2). As-sintered NiTi bulk is composed of both austenite (B2) and martensitic (B19') phases, in the presence of  $\text{Ni}_4\text{Ti}_3$  precipitates. The  $\text{Ni}_4\text{Ti}_3$  precipitates most likely formed during cooling and consumed more nickel atoms than titanium atoms from the matrix. The transformation temperatures of the as-sintered bulk are lower than those of the powder (Figure 3b), indicating nickel depletion in the matrix due to the formation of  $\text{Ni}_4\text{Ti}_3$  precipitates. The  $\text{Ni}_4\text{Ti}_3$  precipitates disappeared in the solution heat treated bulk sample (Figure 3a), suggesting that the solution heat treatment effectively dissolved the  $\text{Ni}_4\text{Ti}_3$  precipitates.

DSC results of NiTi powder and NiTi bulk samples, both as-sintered and solution heat treated, are displayed in Figure 3b. R phase transformation is observed during the austenite (B2) to martensite (B19') transformation of both the NiTi powder and the as-sintered bulk sample. The solution heat treated bulk sample shows single peaks, which are narrower than the peaks of the as-sintered material, indicating a one-step transformation without the R-phase transition. This difference was most likely due to the homogenization

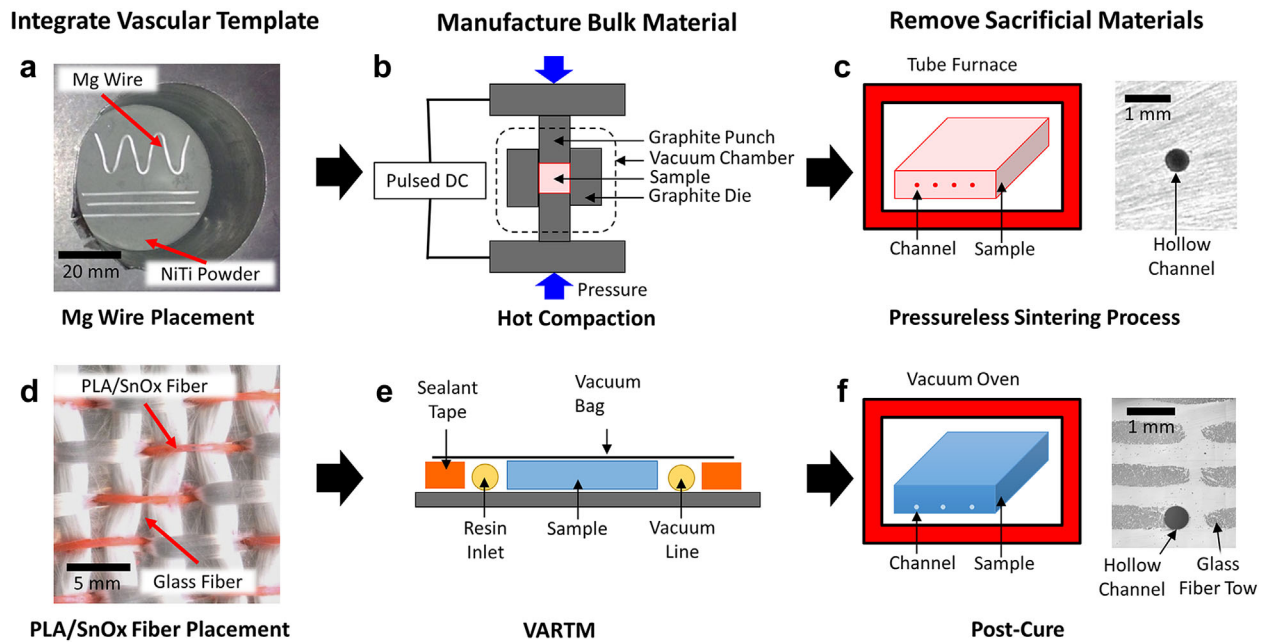


Fig. 2. Outline of vascular specimen fabrication method for the (a–c) SMA and (d–f) PMC divided into three major steps: integration of the vascular template, manufacture of the bulk materials, and removal of sacrificial materials to form channels. (a) Picture of the Mg wire and the first layer of NiTi powder inside the graphite die (dark gray cylinder). (b) Schematic of the SPS process used for hot compaction of the NiTi powder and Mg wire. (c) Schematic of the pressureless sintering and channel formation by evaporation of the Mg wire and a photograph of the resulting 500  $\mu\text{m}$  diameter channel within the SMA sample. (d) Photograph of the woven glass fiber fabric containing PLA/SnOx sacrificial fibers (woven through thickness for visibility). (e) Schematic of the VARTM process used to infiltrate the fiber preform with epoxy. (f) Schematic of the post-cure process used to remove the sacrificial material and an optical micrograph ( $2.5\times$  lens) of the PMC containing a 500  $\mu\text{m}$  channel.

and microstructural recovery that took place during the solution heat treatment procedure.

The martensitic transformation temperatures of the various types of samples are all different from each other, suggesting two observations. First, the martensitic transformation temperatures of the solution heat treated vs. the as-sintered bulk samples are lower, because the dissolution of Ni-rich precipitates enriches the nickel content. The martensitic transformation temperatures of NiTi dramatically decrease with increasing nickel content.<sup>[44]</sup> Second, the martensitic

transformation temperatures of the powder are higher than those of the bulk samples. One possible reason is the existence of a small amount of  $\text{Ni}_4\text{Ti}_3$  precipitates in the powder or oxidation of the bulk samples. In both cases, the amount may be too low to detect by XRD.

### 2.3. Active Cooling Results

Active cooling of the hybrid composite was evaluated using the experimental setup shown schematically in Figure 4. Four testing configurations were evaluated. Two types of

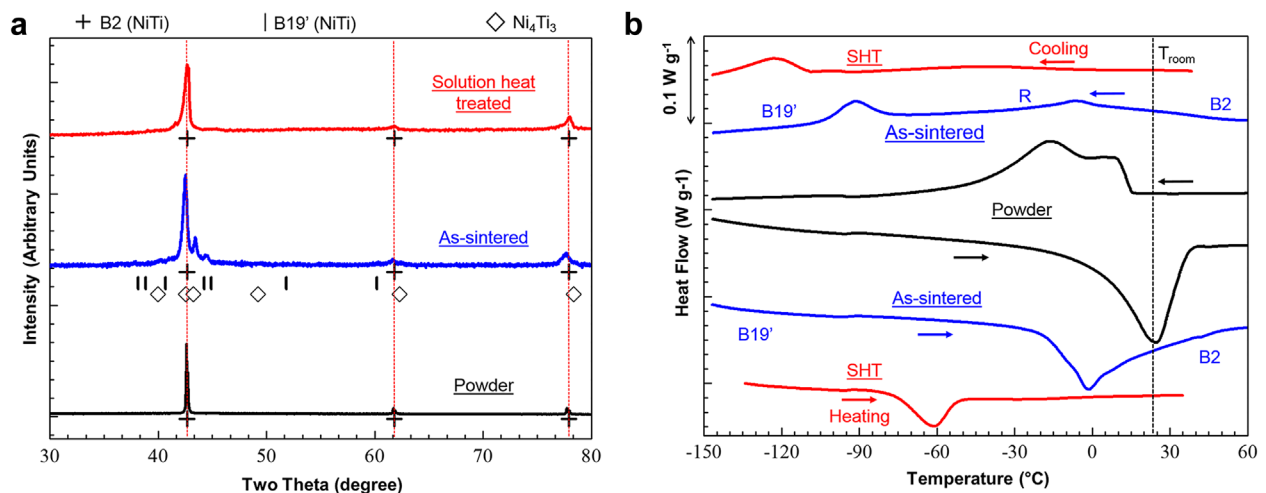


Fig. 3. Material characterization of the NiTi SMA by XRD and DSC testing. (a) XRD data for the NiTi as powder, as-sintered, and solution heat treated (SHT) samples. (b) DSC curves of the NiTi powder and bulk samples, both as-sintered and SHT.

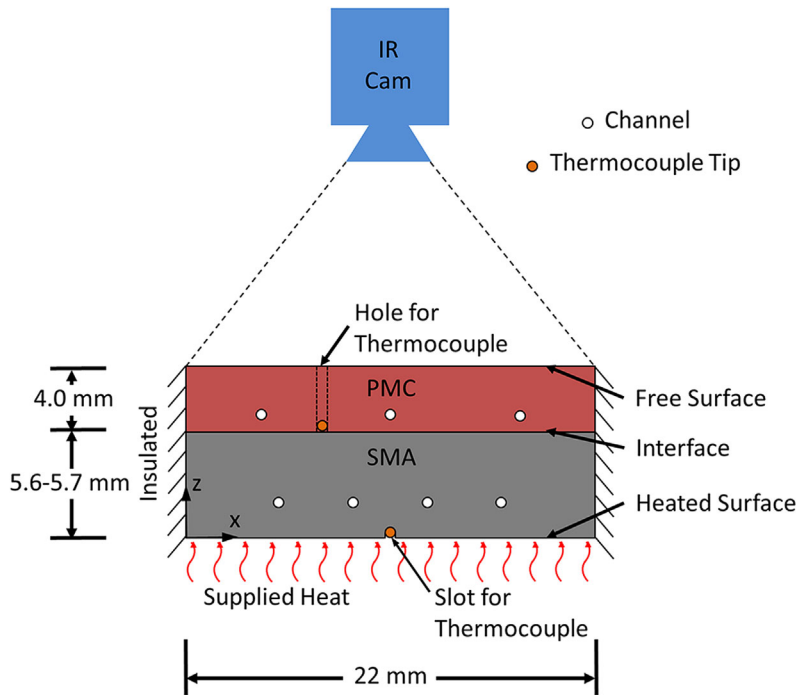


Fig. 4. Schematic of the testing setup for active cooling testing. PMC and SMA specimens are drawn to scale. The setup measures 22 mm in the x-direction and 27 mm in the y-direction. The SMA sample measures 5.6–5.9 mm thick and the PMC sample measures 4.0 mm. Locations for the hole in the PMC for the interface thermocouple and the slot in the SMA for the heated surface thermocouple are marked. In each case the thermocouple was located half way along the length of the specimen (27 mm).

SMA specimens were fabricated with either two or four parallel microchannels embedded. For both types of specimens experiments were conducted with and without active cooling in the vascular PMC layer. The supplied heat flux ( $q_s''$ ) and coolant flow rate ( $Q$ ) were controlled in each test. Coolant was distributed evenly through each of the channels in each material (total coolant flow rate:  $Q_t$ , layer of interest denoted by subscripts PMC or SMA). Sample temperatures ( $T$ ) at the free surface, interface, and heated surface as well as the heat-flux removal rate by the active cooling network ( $q_{ac}''$ ) were recorded. Further details of the experimental setup and analysis can be found in the Experimental Section.

### 2.3.1. Comparison of Non-Cooled versus Actively Cooled System

Active cooling results in vastly reduced temperatures in the hybrid system compared to the cases without cooling (Figure 5). For example, the interface temperature exceeds the  $T_g$  (152 °C by dynamic mechanical analysis, see SI-2 and Figure S3) of the PMC at just 10 kW m<sup>-2</sup> supplied heat flux when no cooling occurs, while the interface remains near room temperature when the system is actively cooled at  $Q_t = 140$  ml min<sup>-1</sup>. When  $q_s'' = 300$  kW m<sup>-2</sup>, the actively cooled temperatures on the heated surface, interface, and free surface were just 179, 98, and 79 °C, respectively. The PMC temperatures are well below the maximum service temperature. The NiTi temperature is high enough that superelastic behavior

may be affected, but well below the 500 °C threshold for superelasticity in high temperature SMAs. The temperature of the NiTi is preserved below 150 °C, the maximum temperature for superelasticity in equiatomic NiTi, to approximately  $q_s'' = 230$  kW m<sup>-2</sup>. Without active cooling the PMC substrate would be destroyed by thermal decomposition and the NiTi would have substantially changed phase transformation characteristics and degraded mechanical properties at  $q_s'' = 300$  kW m<sup>-2</sup>.

### 2.3.2. Effect of Channel Distribution

Active cooling effectiveness strongly depends on the distribution of the cooling channels within the system. Figure 6 shows the sample temperature at different locations in the hybrid laminate, heat-flux removal rate, and free surface temperature profiles from IR imaging for each of the channel configurations with equal total flow rate through the SMA.

The four channel SMA cooled more effectively than the two channel SMA, both with and without cooling through the PMC. The IR temperature profiles show that the free surface temperature is both more uniform and lower when cooling through four channels in the SMA compared to two. The heat-flux removal rate is also higher for the four channel SMA test cases than their respective two channel SMA cases.

Active cooling through the PMC substantially reduces the temperature at the interface and free surface, with only a small

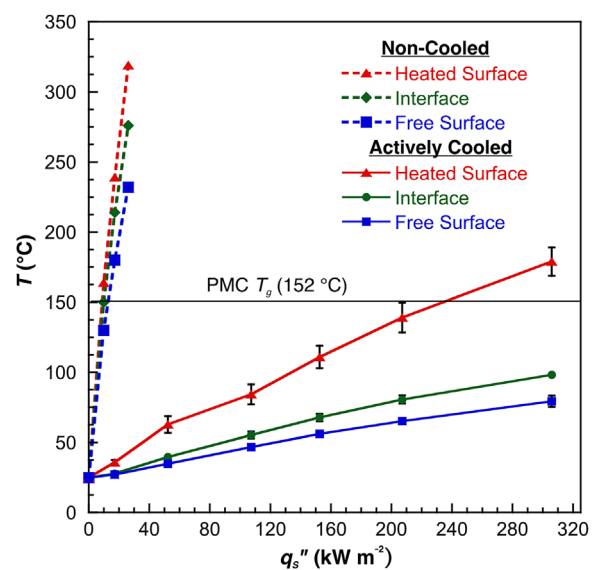


Fig. 5. Comparison of sample temperatures with and without active cooling as a function of supplied heat flux. Active cooling results are shown for the four channel SMA specimen with PMC cooling and  $Q_t = 140$  ml min<sup>-1</sup> of water. Active cooling results represent the average of two thermal tests, with the error bars equivalent to the range of the data. Non-cooled results are shown for a single test.

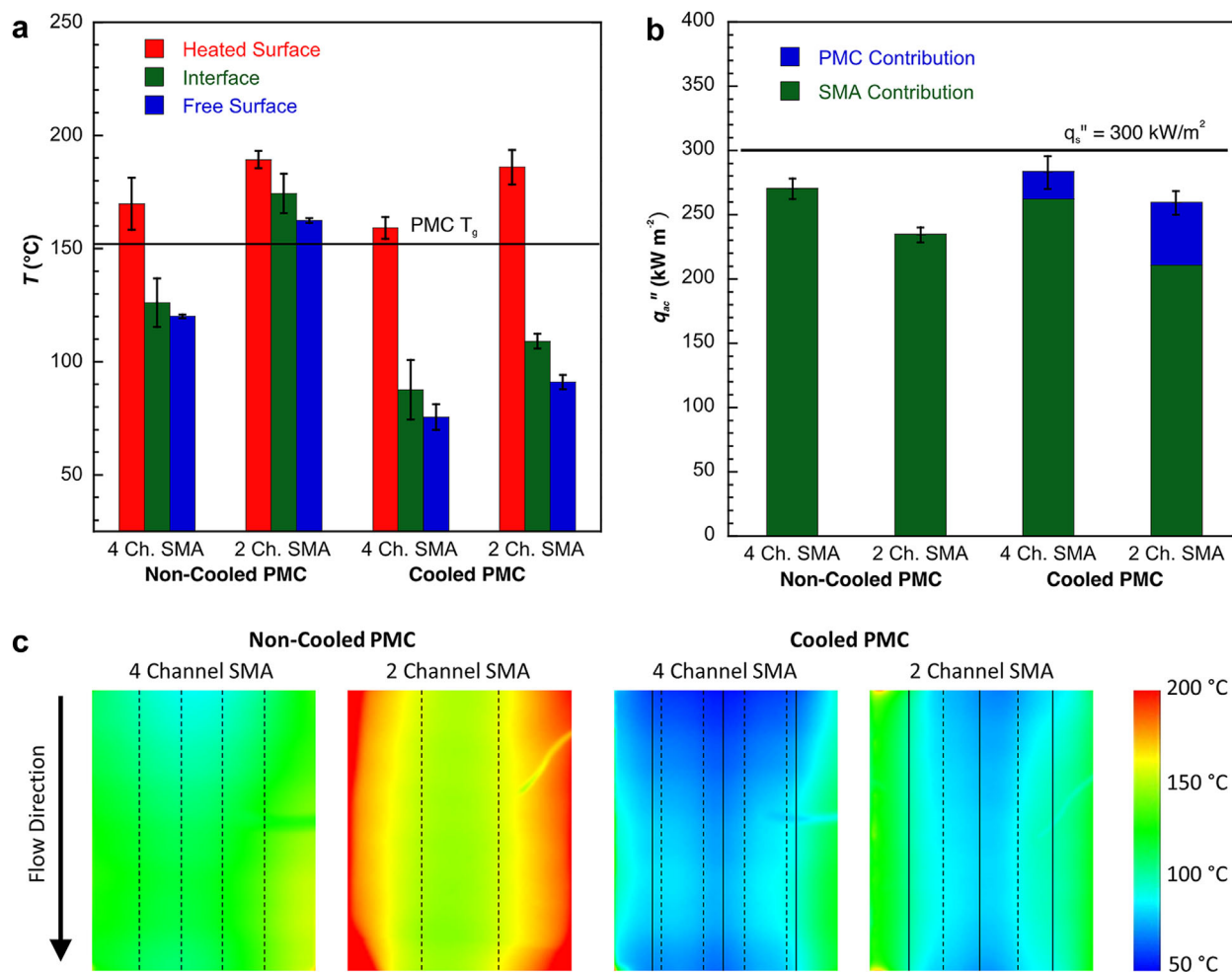


Fig. 6. Thermal performance summary of all testing configuration. (a) Measured temperature of the heated surface, interface, and free surface. (b) Heat flux removed by active cooling. (c) Free surface temperature profiles from IR for each testing configuration. Channel locations are marked in the IR images, with the SMA channels shown as dashed lines and the PMC channels as solid lines. Notes:  $q''_s = 300 \text{ kW m}^{-2}$  and  $Q_{l,SMA} = 80 \text{ ml min}^{-1}$  in the SMA for all cases. When the PMC was cooled,  $Q_{l,PMC} = 60 \text{ ml min}^{-1}$  in the PMC. The coolant was water. Data represents the average of three thermal tests with error bars equal to one standard deviation. The thermocouple wire is visible on the right side of several of the IR images.

change to the heated surface temperature. For the two channel SMA case, the addition of active cooling in the PMC reduced the interface temperature below  $T_g$  of the PMC. In fact, the interface and free surface temperatures were lower in this case than the four channel SMA without PMC cooling. For the same flow rate in the SMA, the SMA's contribution to the heat-flux removal rate slightly reduces when the PMC is cooled. However, total heat-flux removal rate slightly increases from the added contribution of the actively cooled PMC.

The effect of flow rate on sample temperatures and heat-flux removal rate with and without cooling through the PMC is presented in Figure 7. In this case the flow is distributed equally among the four SMA channels and three PMC channels. All temperatures decrease non-linearly with flow rate, with the largest decreases at low flow rate. The free surface temperature mirrors the interface temperature and was not included in the graph. Heat-flux removal rate is fairly flat with a slight increase with increased flow rate. Rerouting a

portion of the coolant through the PMC causes a small increase in the heated surface temperature, but significantly reduces the interface temperature. The heat-flux removal rate show no notable differences between the cooled and non-cooled PMC within experimental scatter.

### 2.3.3. Effect of Coolant Media

In many cases water cannot be used as a coolant media due to its electrical conductivity. A common dielectric coolant is polyalphaolefin (PAO) oil. Figure 8 reveals the effect of cooling with PAO in comparison to water. Both the heated surface and interface temperatures are much higher when cooling with PAO oil than with water. When cooling with PAO oil the interface temperature never falls below  $200^\circ\text{C}$ , well above the  $T_g$  ( $152^\circ\text{C}$ ) of the PMC. Heat-flux removal rate is no different for water and PAO. Thus, the difference in cooling performance is attributed to the lower specific heat capacity and thermal conductivity of PAO in comparison to water

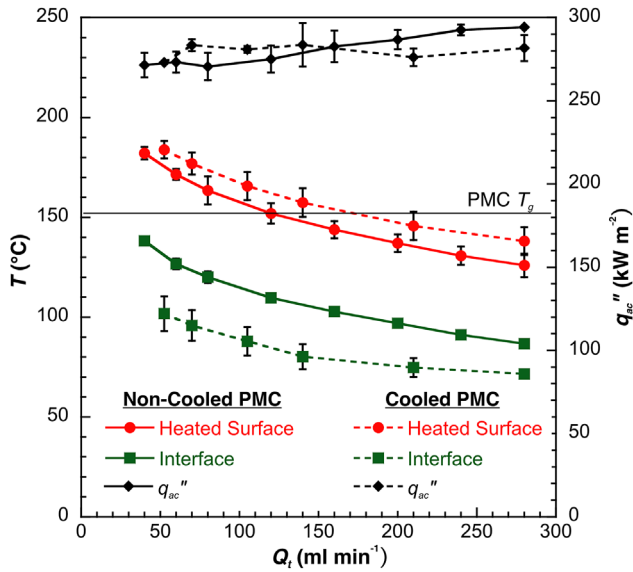


Fig. 7. Effect of total coolant flow rate on heat-flux removal rate and sample temperature. Testing configurations consisted of the four-channel SMA both with and without active cooling in the PMC for a supplied heat flux of  $q''_s = 300 \text{ kW m}^{-2}$ . The coolant was water. Data represents the average of two tests with the error bars equivalent to the range of the data.

(Table S1). A lower specific heat capacity leads to higher fluid temperature for the same level of heat extraction. For example, at  $Q_t = 70 \text{ ml min}^{-1}$  and  $q''_s = 300 \text{ kW m}^{-2}$  for the four channel SMA with cooled PMC, the PAO fluid temperature was  $134^\circ\text{C}$  compared to  $75^\circ\text{C}$  for water. In addition, PAO oil viscosity is about 5–6 $\times$  that of water, requiring significantly more power to pump through the specimen.

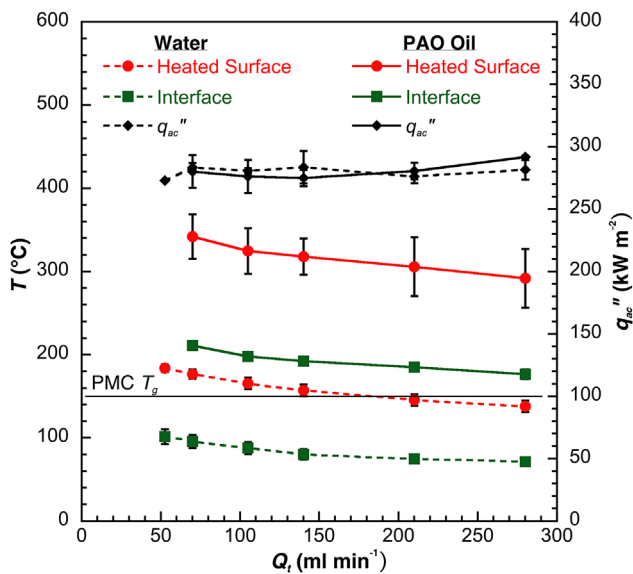


Fig. 8. Effect of coolant media (PAO oil vs. water) on cooling performance. Testing configuration consisted of four-channel SMA with active cooling through the PMC for  $q''_s = 300 \text{ kW m}^{-2}$ . Data represents the average of two tests with error bars equal to the range of the data.

### 3. Conclusion

Cooling channels were fabricated in each phase of a shape memory alloy (SMA)–polymer matrix composite (PMC) hybrid material using the VaSC processing technique. A previously reported sacrificial material composed of poly(lactic acid)/tin(II) oxalate fibers was used for the PMC. For the SMA, a new approach using Mg wire as the sacrificial material was developed and shown to successfully create microchannels in NiTi. XRD and DSC results show the shape memory characteristics of the SMA are preserved, but with reduced transformation temperatures after the VaSC process.

Active cooling dramatically reduced the sample temperatures in the vascularized bilayer hybrid material. Without active cooling, the specimen only sustained a heat flux of  $10 \text{ kW m}^{-2}$  before the temperature in the PMC exceeded  $T_g$ . In contrast, the actively cooled specimen maintained the PMC temperature below  $T_g$  when subjected to  $300 \text{ kW m}^{-2}$  heat flux at the NiTi surface. Active cooling was more effective when coolant was distributed through more channels in the SMA specimen (4 vs. 2). Furthermore, distributing some of the coolant through channels in the PMC also reduced the interface (SMA/PMC) temperature. Cooling with water resulted in lower sample temperatures than cooling with PAO oil.

Vascularization enables additional functionality through the introduction of different fluids. While active cooling was demonstrated in this study, functions such as self-healing and damage detection in metals are future targets for vascular technology. Future work should be conducted to explore if the approach for manufacturing vascular NiTi is suitable to other sintered metals by appropriately selecting the sacrificial material composition.

### 4. Experimental Section

#### 4.1. Vascular SMA Fabrication

Pre-alloyed NiTi powder with a nominal composition of 50.4 at % Ni and a purity of 99.9% (Nanoval) was used as the matrix material. The powder was sieved to obtain particles below  $53 \mu\text{m}$  diameter. The particles are nearly spherical, have smooth surfaces, and are surrounded by small satellites indicating that the powder was produced by gas atomization (Figure S1). Mg wires with a purity of 99.8% (Weihaio Magnesium Corp.) were used as the sacrificial template for microchannels.

The process for fabricating the vascularized SMA specimens is summarized in Figure 2a–c. Two layers of the NiTi powder were poured into a 50 mm diameter graphite die, sandwiching 2 or 4 parallel  $500 \mu\text{m}$  diameter Mg wires. The wires were manually pushed into the powder after being placed onto the first layer of powder to ensure location. The Mg-wire/NiTi was hot compacted in a spark plasma sintering (SPS) system (GT Advanced Technologies, Model 25-10). The chamber was evacuated and held at  $10^{-6}$  torr for 10 min before heating. DC current was applied, increasing from 0 to 1 250 A in 4 min and then stabilized at 860 A for 10 min at  $500^\circ\text{C}$  under 50 MPa uniaxial compaction pressure. The pulse cycle was 10 ms on and 10 ms off and the heating rate was  $200^\circ\text{C min}^{-1}$ . Graphite foils were applied between the samples and graphite die. The temperature was

measured in a drilled hole in the bottom graphite punch, which was immediately below the surface that was in contact with the sample.

Following SPS, the Mg-wire/NiTi compacts were pressureless sintered under vacuum ( $10^{-3}$  torr) at 1270 °C in a tube furnace under flowing ultra-high-purity argon; the detailed procedures of pressureless sintering are described in Hu et al.<sup>[45]</sup> Mg powder (Weihao Magnesium Corp.) was placed around the Mg-wire/NiTi compacts before pressureless sintering to absorb the remaining oxygen in the environment. After pressureless sintering, the samples were gradually cooled under flowing argon in the furnace to room temperature over 2.5 h.

The resulting SMA specimen contained vascular channels resulting from the vaporization of the Mg wire. Precipitates were observed in the as-sintered bulk sample. In order to dissolve these precipitates, the as-sintered bulk sample was solution heat treated. The NiTi sample was wrapped in a tantalum foil and sealed in a quartz tube under vacuum then placed in the box furnace for the solution heat treatment at 900 °C for 1 h. After treatment, the specimen still in the quartz tube was quenched in ice water. The quartz tube stayed intact until fully quenched, so that NiTi stays in vacuum throughout the heat treatment and quenching processes to avoid oxidation. The tantalum foil removes residual oxygen in the quartz tube and prevents reaction between the NiTi and the quartz tube.

Specimens were cut to  $22 \times 27$  mm<sup>2</sup> using electrical discharge machining, with the channels running along the 27 mm length. Thickness varied from 5.6 to 5.9 mm. Channels were spaced 4 mm apart in the four channel specimen and 7 mm apart in the two channel specimen, with channels located 2.0 mm from the bottom surface.

#### 4.2. Vascular PMC Manufacture

Channel fabrication in the PMC is summarized in Figure 2d–f. Sacrificial fibers were prepared from 500 μm diameter PLA monofilament fiber (Nextfusion Inc.) treated with tin(II) oxalate catalyst using a modified procedure introduced by Esser Kahn et al.<sup>[14]</sup> and Dong et al.<sup>[18]</sup> See SI-1 for details on this process. PMC specimens were manufactured from a single layer of 3D orthogonally woven S-2 glass fiber textile (Team Inc.) (Figure S2). Sacrificial fibers were manually incorporated by hand using a sewing needle. The sacrificial fibers were placed in the bottom most warp layer between the tows and ran straight along the warp tow. No glass fibers were removed to accommodate the sacrificial fibers.

The textile, including the sacrificial fibers, was infused with EPON 862/EPIKURE W epoxy (mixed 100:26.4 by mass, Momentive Specialty Chemicals Inc.), using vacuum assisted resin transfer molding. The resin was pre-heated then degassed at 70 °C for 2 h, while the preform was pre-heated to 100 °C. The infusion was conducted in a convection oven at 100 °C then the composite was cured at 121 °C for 8 h, with a  $3^\circ\text{C min}^{-1}$  warming rate and a  $1^\circ\text{C min}^{-1}$  cooling rate. Sacrificial components were removed from the composites using a VaSC treatment at 200 °C under vacuum for 24 h. The composite had an average fiber volume of  $44.5 \pm 1.3\%$  measured by matrix burn-off.

Specimens contained three channels placed 7 mm apart and 0.9 mm from the bottom surface. Specimens were cut to  $22 \times 27$  mm<sup>2</sup> using a diamond blade wet saw, with the channels running along the 27 mm length. PMC thickness was 4.0 mm.

#### 4.3. Shape Memory Alloy Characterization

The phase composition of the NiTi powder and bulk NiTi with micro-channels was determined using an XRD (D8 Discover, Bruker,

WI, USA) with Cu  $K\alpha$  radiation (wavelength = 1.542 Å) at 40 kV and 30 mA. The two theta range was varied from 30° to 80° with a step size of 0.04° and a step time of 1.5 s. Data were collected at room temperature. The identification of phase was done according to the Joint Committee on Powder Diffraction Standards (JCPDS) card number 19-0850 for B2 (austenite NiTi), 27-0344 for B19' (martensite NiTi), and ICSD collection code 166371 for Ni<sub>4</sub>Ti<sub>3</sub>.

Phase transformation behavior of the bulk NiTi with micro-channels and the NiTi powder was compared using a differential scanning calorimeter (DSC, TA Instruments, Model Q20) on 20–80 mg specimens. The temperature was ramped from  $-150$ – $100$  °C at a heating rate of  $10^\circ\text{C min}^{-1}$ . Tests were conducted in a nitrogen environment with a flow rate of  $50\text{ mL min}^{-1}$ . Two tests were conducted for repeatability, and each test consists of 3 cycles of heating and cooling. Transformation temperatures were determined from the peaks using the slope line extension method.<sup>[46]</sup>

#### 4.4. Active Cooling Characterization

Active cooling of the hybrid composite was evaluated using the test arrangement shown schematically in Figure 4. Heat was provided from a heater composed of a copper block measuring  $22 \times 27 \times 15$  mm<sup>3</sup> in height containing two 200 W (6.35 mm diameter, 38.1 mm long) high-temperature cartridge heaters (Tutco Heating Solutions Group) spaced 10 mm apart and oriented along the  $y$ -axis. The voltage supplied to the heater was controlled via a Variac variable transformer (Staco Energy Products Co., Type L1010) and measured using a multimeter (Fluke Inc., Model 179). The SMA was bonded to the surface of the copper using high temperature cement (Rutland Fire Clay Company, Rutland Black). The SMA and PMC specimens were bonded together with a thin layer of thermal epoxy (Aavid Thermalloy, Ther-O-Bond 1600-40, thermal conductivity =  $0.85\text{ W m}^{-1}\text{ K}^{-1}$ ). The bottom of the heater and sides of the heater and sample were insulated using approximately 25 mm of calcium silicate insulation. The top surface of the PMC was open to the atmosphere.

The average temperature of the free surface was measured using an IR camera (FLIR, Model SC620) calibrated to an accuracy of  $\pm 2^\circ\text{C}$ . The free surface was painted flat black to ensure uniform emissivity of 0.95. The interface temperature between the PMC and the SMA was measured using an E-type thermocouple (Omega Engineering, Model EMQSS-020U) placed in a small hole drilled through the thickness of the PMC. The temperature of the heated face of the SMA was measured using a K-type thermocouple (Omega Engineering, Model KMQXL-020U) inserted into a 0.50 mm square slot machined into the SMA using electrical discharge machining. K-type and E-type thermocouples have an accuracy of  $\pm 1.1$  and  $\pm 1.0^\circ\text{C}$ , respectively. Thermocouple data were collected using temperature sensors (Phidgets Inc., Model 1048) and recorded using a custom LabVIEW code (National Instruments) at 1 Hz continuously.

Two coolants were used for testing, including water and polyalphaolefin (PAO) oil (MIL-PRF-87252), a dielectric coolant. Coolant was pumped through each channel separately to ensure even flow using a peristaltic pump (Cole-Parmer Masterflex, Model EW-07551-00), which powered up to eight separate pump heads. The coolant supply was maintained at room temperature ( $20$ – $22^\circ\text{C}$ ). The fluid delivery channels were connected to the specimen via 19 gage syringe needles inserted into 1 mm diameter, 1 mm deep holes drilled into the ends of each specimen. The temperature of the fluid just before and after traveling through the specimen was measured using T-type thermocouples (Omega Engineering, Model TMQSS-020U) inserted into the tubing in the center of the flow. T-type

thermocouples were rated with an accuracy of  $\pm 0.5^\circ\text{C}$ . Note that the thermocouple accuracy is a significant source of error in calculating heat-flux removal rate, particularly at high flow rates (see Figure S4).

In a typical testing procedure coolant was pumped through the selected channels, then the heater was turned on. The system was allowed to reach a steady state and measurements were recorded. Two to three tests were conducted on each specimen to examine repeatability, while cooling the specimen down to room temperature between tests.

#### 4.5. Active Cooling Analysis

The heat flux supplied by the heater was calculated from the electrical power supplied,

$$q_s'' = \frac{V^2}{AR}, \quad (1)$$

where  $V$  is the voltage supplied to the heater,  $A$  is the cross-sectional area of the heater and specimen ( $2.2 \times 2.7$  cm), and  $R$  is the resistance of the heater. The heater resistance varied from  $38.6\ \Omega$  at room temperature to  $40.0\ \Omega$  at heater temperature of  $500^\circ\text{C}$ . The heat removed by active cooling is calculated from the change in temperature of the coolant from inlet to outlet ( $\Delta T$ ) in each channel ( $n$ ) as

$$q_{ac}'' = \sum_{i=1}^n \left( \frac{\dot{m} c_p \Delta T}{A} \right)_i, \quad (2)$$

where  $\dot{m}$  is the mass flow rate,  $c_p$  is the specific heat capacity of the coolant. The heat removal was calculation separately for the SMA and PMC. The two values were totaled to obtain the total heat removal. Variation of coolant properties with temperature was calculated using an interpolation of manufacturer's data for PAO oil and tabulated values for water. Thermal data for the coolant at  $40^\circ\text{C}$  and  $100^\circ\text{C}$  is given in Table S1.

Article first published online: xxxx  
Manuscript Revised: February 19, 2016  
Manuscript Received: January 13, 2016

- [1] E. A. Meese, H. Nørstrud, *Aerosp. Sci. Technol.* **2002**, *6*, 185.
- [2] R. Mahajan, C.-P. Chiu, G. Chrysler, *Proc. IEEE* **2006**, *94*, 1476.
- [3] J. Park, X. Li, *J. Power Sources* **2006**, *162*, 444.
- [4] S. Yu, D. Jung, *Renew. Energy* **2008**, *33*, 2540.
- [5] Z. Rao, S. Wang, *Renew. Sustain. Energy Rev.* **2011**, *15*, 4554.
- [6] Y. Wang, G. Yuan, Y.-K. Yoon, M. G. Allen, S. A. Bidstrup, *IEEE Trans. Compon. Packag. Technol.* **2005**, *28*, 477.
- [7] D. Hengeveld, M. Mathison, J. Braun, E. Groll, A. Williams, *HVACR Res.* **2010**, *16*, 189.
- [8] M. E. Lyall, A. D. Williams, B. J. Arrit, B. S. Taft, in *49th AIAA/ASME/ASCE/AHS/ASC Structures, Structural Dynamics, and Materials Conference*; AIAA: Schaumburg, Illinois USA **2008**.
- [9] A. D. Williams, R. L. Underwood, B. J. Arrit, G. T. Busch, B. S. Taft, in *51st AIAA/ASME/ASCE/AHS/ASC Structures, Structural Dynamics, and Materials Conference*; AIAA: Orlando, Florida USA **2010**.
- [10] K. S. Toohey, N. R. Sottos, J. A. Lewis, J. S. Moore, S. R. White, *Nat. Mater.* **2007**, *6*, 581.
- [11] H. R. Williams, R. S. Trask, I. P. Bond, *Compos. Sci. Technol.* **2008**, *68*, 3171.
- [12] A. R. Hamilton, N. R. Sottos, S. R. White, *Adv. Mater.* **2010**, *22*, 5159.
- [13] C. J. Norris, G. J. Meadway, M. J. O'Sullivan, I. P. Bond, R. S. Trask, *Adv. Funct. Mater.* **2011**, *21*, 3624.
- [14] A. P. Esser-Kahn, P. R. Thakre, H. Dong, J. F. Patrick, V. K. Vlasko-Vlasov, N. R. Sottos, J. S. Moore, S. R. White, *Adv. Mater.* **2011**, *23*, 3654.
- [15] A. S. Wu, A. M. Coppola, M. J. Sinnott, T.-W. Chou, E. T. Thostenson, J.-H. Byun, B.-S. Kim, *Compos. Sci. Technol.* **2012**, *72*, 1618.
- [16] J. W. C. Pang, I. P. Bond, *Compos Part A* **2005**, *36*, 183.
- [17] J. W. C. Pang, I. P. Bond, *Compos. Sci. Technol.* **2005**, *65*, 1791.
- [18] H. Dong, A. P. Esser-Kahn, P. R. Thakre, J. F. Patrick, N. R. Sottos, S. R. White, J. S. Moore, *ACS Appl. Mater. Interfaces* **2012**, *4*, 503.
- [19] R. C. R. Gergely, S. J. Pety, B. P. Krull, J. F. Patrick, T. Q. Doan, A. M. Coppola, P. R. Thakre, N. R. Sottos, J. S. Moore, S. R. White, *Adv. Funct. Mater.* **2015**, *25*, 1043.
- [20] S. Soghrati, P. R. Thakre, S. R. White, N. R. Sottos, P. H. Geubelle, *Int. J. Heat Mass Transf.* **2012**, *55*, 5309.
- [21] S. Soghrati, A. R. Najafi, J. H. Lin, K. M. Hughes, S. R. White, N. R. Sottos, P. H. Geubelle, *Int. J. Heat Mass Transf.* **2013**, *65*, 153.
- [22] D. M. Phillips, M. Ryan Pierce, J. W. Baur, *Compos. Part A* **2011**, *42*, 1609.
- [23] A. Kousourakis, M. K. Bannister, A. P. Mouritz, *Compos. Part A* **2008**, *39*, 1394.
- [24] C.-Y. Huang, R. S. Trask, I. P. Bond, *J. R. Soc. Interface* **2010**, *7*, 1229.
- [25] A. M. Coppola, P. R. Thakre, N. R. Sottos, S. R. White, *Compos. Part A* **2014**, *59*, 9.
- [26] C. J. Norris, I. P. Bond, R. S. Trask, *Compos. Sci. Technol.* **2011**, *71*, 847.
- [27] A. Kousourakis, A. P. Mouritz, M. K. Bannister, *Compos. Struct.* **2006**, *75*, 610.
- [28] G. P. McCombe, J. Rouse, R. S. Trask, P. J. Withers, I. P. Bond, *Compos. Part A* **2012**, *43*, 613.
- [29] C. J. Norris, I. P. Bond, R. S. Trask, *Compos. Part A* **2011**, *42*, 639.
- [30] J. Ma, I. Karaman, R. D. Noebe, *Int. Mater. Rev.* **2010**, *55*, 257.
- [31] H. Sehitoglu, J. Jun, X. Zhang, I. Karaman, Y. Chumlyakov, H. J. Maier, K. Gall, *Acta Mater.* **2001**, *49*, 3609.
- [32] L. Hu, A. Kothalkar, G. Proust, I. Karaman, M. Radovic, *J. Alloys Compd.* **2014**, *610*, 635.

- [33] A. Kothalkar, R. Benitez, L. Hu, M. Radovic, I. Karaman, *Met. Mater. Trans. A* **2014**, *45*, 2646.
- [34] F. Cheng, L. Hu, J. N. Reddy, I. Karaman, E. Hoffman, M. Radovic, *Acta Mater.* **2014**, *68*, 267.
- [35] G. Williams, R. Trask, I. Bond, *Compos. Part A* **2007**, *38*, 1525.
- [36] P. J. Kwok, S. M. Oppenheimer, D. C. Dunand, *Adv. Eng. Mater.* **2008**, *10*, 820.
- [37] D. J. Jorgensen, D. C. Dunand, *Mater. Sci. Eng. Struct. Mater. Prop. Microstruct. Process.* **2010**, *527*, 849.
- [38] D. J. Jorgensen, D. C. Dunand, *Acta Mater.* **2011**, *59*, 640.
- [39] A. J. Neurohr, D. C. Dunand, *Acta Mater.* **2011**, *59*, 4616.
- [40] A. J. Neurohr, D. C. Dunand, *Acta Biomater.* **2011**, *7*, 1862.
- [41] A. Bansiddhi, D. C. Dunand, *Adv. Eng. Mater.* **2011**, *13*, 301.
- [42] T. Aydogmus, S. Bor, *J. Alloys Compd.* **2009**, *478*, 705.
- [43] T. Aydogmus, E. T. Bor, S. Bor, *Metall. Mater. Trans. Phys. Metall. Mater. Sci.* **2011**, *42A*, 2547.
- [44] K. Otsuka, X. Ren, *Prog. Mater. Sci.* **2005**, *50*, 511.
- [45] L. Hu, R. Benitez, S. Basu, I. Karaman, M. Radovic, *Acta Mater.* **2012**, *60*, 6266.
- [46] ASTM, *ASTM Int.* **2004**, *F2004-05*.
-